

Cross sections and photoelectron angular distributions in photodetachment from negative ions using equation-of-motion coupled-cluster Dyson orbitals

C. Melania Oana, and Anna I. Krylov

Citation: *The Journal of Chemical Physics* **131**, 124114 (2009); doi: 10.1063/1.3231143

View online: <https://doi.org/10.1063/1.3231143>

View Table of Contents: <http://aip.scitation.org/toc/jcp/131/12>

Published by the *American Institute of Physics*

Articles you may be interested in

[Dyson orbitals for ionization from the ground and electronically excited states within equation-of-motion coupled-cluster formalism: Theory, implementation, and examples](#)

The Journal of Chemical Physics **127**, 234106 (2007); 10.1063/1.2805393

[Angular Distribution of Photoelectrons](#)

The Journal of Chemical Physics **48**, 942 (1968); 10.1063/1.1668742

[Calculation of photodetachment cross sections and photoelectron angular distributions of negative ions using density functional theory](#)

The Journal of Chemical Physics **143**, 144310 (2015); 10.1063/1.4932978

[Quantum scattering studies of electronically inelastic collisions of CN \(\$X^2\Sigma^+\$, \$A^2\Pi\$ \) with He](#)

The Journal of Chemical Physics **91**, 5425 (1989); 10.1063/1.457570

[Velocity map imaging of ions and electrons using electrostatic lenses: Application in photoelectron and photofragment ion imaging of molecular oxygen](#)

Review of Scientific Instruments **68**, 3477 (1997); 10.1063/1.1148310

[Microwave spectra, structure, and dynamics of the weakly bound complex, \$N_2CO_2\$](#)

The Journal of Chemical Physics **133**, 244303 (2010); 10.1063/1.3517061

PHYSICS TODAY

WHITEPAPERS

ADVANCED LIGHT CURE ADHESIVES

Take a closer look at what these environmentally friendly adhesive systems can do

READ NOW

PRESENTED BY



Cross sections and photoelectron angular distributions in photodetachment from negative ions using equation-of-motion coupled-cluster Dyson orbitals

C. Melania Oana^{a)} and Anna I. Krylov^{b)}*Department of Chemistry, University of Southern California, Los Angeles, California 90089-0482, USA*

(Received 8 July 2009; accepted 27 August 2009; published online 25 September 2009)

We report total and differential cross sections for photodetachment from negative ions using Dyson orbitals calculated from equation-of-motion coupled-cluster wave functions and free wave description of the detached electron. The energy dependence of the cross sections is reproduced well, however, the accuracy of absolute values varies. For F^- , C^- , NH_2^- , and H^- , the calculated cross sections are within the error bars from the experimental values, whereas the errors for Li^- and OH^- are about 20%. The largest errors are observed for O^- and O_2^- for which the calculated cross sections differ from the experimental ones by factors of 3 and 2, respectively. Calculated anisotropy parameters for atomic anions exhibit too slow decrease, which suggests that the diffuseness of the computed Dyson orbitals is underestimated. Moreover, in the asymptotic region, the orbitals exhibit artifactual oscillations probably due to the limitations of Gaussian basis sets. The analysis of the trends in the experimental anisotropy parameters suggests that the interaction of the detached electron with the core, which is neglected in the present model, is important. © 2009 American Institute of Physics. [doi:10.1063/1.3231143]

I. INTRODUCTION

Numerous variations of photoelectron spectroscopy are capable of providing detailed information about the electronic structure of molecules and ions, as well as their interactions with light.^{1–9} Kinetic energy distribution of photoelectrons contains information about electronic and vibrational levels, which, in turn, depend on the potential energy surfaces (PESs) of the species involved. The analysis of Franck–Condon progressions allows one to determine structural differences between the initial and ionized/detached states, as well as to infer changes in the electronic wave functions. A well-resolved photoelectron spectrum is a unique signature of a system, however, even integrated Franck–Condon progressions, such as photoionization efficiency spectra, can be used to identify and distinguish species.

Wealth of the information can be obtained by considering only the vibrational part of the Franck–Condon factors (FCFs) under simple assumptions about the electronic component of the total cross sections.^{10,11} However, the interpretation of some experiments requires more precise knowledge of the electronic part of the cross section. For example, measurements of electron affinities (EAs) or ionization energies (IEs) rely on the near-threshold photoelectrons, and extracting EAs (or IEs) are based on the energy dependence of the cross section. Distinguishing isomers by their photoionization efficiency spectra is also more reliable when the elec-

tronic part of the cross section is known.^{12,13} Thus, modeling of the electronic part of the photoionization and/or photodetachment cross sections is complementary to the calculations of FCFs. More detailed information about electronic wave functions can be obtained by measuring angular distributions of photoelectrons (PADs), which are related to differential cross sections.

A central quantity for calculating total and differential cross sections is photoelectron matrix element connecting the initial and the final wave functions:

$$D_k^{IF} = \mathbf{u} \langle \Psi_I^N | \mathbf{r} | \Psi_F^{N-1} \cdot \Psi_k^{\text{el}} \rangle = \langle \phi_{IF}^d | r_u | \Psi_k^{\text{el}} \rangle \quad (1)$$

where \mathbf{u} is a unit vector in the direction of laser polarization, Ψ_k^{el} is a final state of the free electron with energy corresponding to the wave vector k , i.e., $E_{\text{el}}(k) = k^2/2$, and ϕ_{IF}^d is the so called Dyson orbital that contains all the necessary information about the wave functions of the initial N -electron system and the remaining $N-1$ electron core:

$$\phi_{IF}^d(1) = \sqrt{N} \int \Psi_I^N(1, \dots, n) \Psi_F^{N-1}(2, \dots, n) d2 \dots dn. \quad (2)$$

Dyson orbitals ϕ^d are employed in calculations of Compton profiles,¹⁴ electron momentum spectra,^{15,16} and interpretation of orbital imaging experiments.^{17–19} Although Dyson orbitals defined by Eq. (2) can be computed for any initial and final many-electron wave functions,^{20,21} many theoretical studies employ an independent-particle approximation and treat ϕ^d within the Hartree–Fock/Koopmans frame-

^{a)}Electronic mail: oana@usc.edu.

^{b)}Author to whom correspondence should be addressed. Electronic mail: krylov@usc.edu.

work. In more rigorous studies, correlation effects have been taken into account using Green functions and propagator formalism.^{22–25}

Recently, we presented the calculation of Dyson orbitals within equation-of-motion coupled-cluster (EOM-CC) formalism.²⁶ In chemical applications, EOM theory has been adapted from nuclear physics²⁷ for calculating electronically excited states^{28–31} and later extended to EAs and ionization potentials.^{32–34} Subsequent developments^{35–43} of the EOM methodology with a CC reference wave function enabled accurate calculations of electron attached, ionized, and spin-flipped states, as discussed in detail in several reviews.^{44–52}

By combining different EOM-CC methods, one can describe ionization from open-shell and electronically excited states.⁵¹ Calculated using highly correlated wave functions, EOM-CC Dyson orbitals include both correlation and orbital relaxation effects. For ionizations from the ground state of closed-shell molecules, these effects often manifest themselves not in the shape of the orbitals (e.g., we observed that the CCSD Dyson orbitals are often very similar to the canonical Hartree–Fock ones, except when there is strong mixing of Koopmans configurations⁵³), rather in the norms of the Dyson orbitals, which are related to the absolute cross sections via Eq. (1). The focus of this work is on the second aspect of the problem, that is, the ionized electron. As the first step, we employ a simple plane wave description of photoelectrons, as in Ref. 54, to benchmark the performance of this model for photodetachment from negative ions. In these processes, the remaining core is neutral, and one can expect that the plain-wave description of photoelectrons (as well as other assumptions of our model described below) are better justified compared to the ionization of the neutrals. In this paper, we consider several atomic and small molecular ions, and compute total cross sections and the anisotropy parameter β . The comparison with the experimental data is used to determine the accuracy of this approach and to validate the assumptions of the model.

The field of anion spectroscopy has grown steadily, as demonstrated by a large number of extensive studies of inorganic, organic, metal-organic, and cluster anions.^{55–70} The development of new high resolution techniques expanded the applicability of photodetachment experiments to include electronic structure determination of unstable and excited states, photodetachment ultrafast dynamics, anion reactivity, and intermolecular interactions in cluster anions.^{3,8,71–74}

On the theory side, several models of varying complexity have been developed,^{54,75–77} and the applications revealed their capabilities and limitations. Most importantly, testing the predictions of these models against the experimental measurements helped quantify the relative importance of different effects and interactions involved in the photoionization process. For example, for atomic ionization, the Cooper–Zare formula^{75,78} derived within central-potential model captures correctly the so-called geometrical effects resulting from angular momentum conservation laws and allows one to account for possible phase shifts between the partial waves (more on this in Sec. II C). Whereas in a general case the predictions of the Cooper–Zare model are subject to the uncertainties in the parameters used (dipole radial

matrix elements and phase shifts), some limiting situations afford simple analytic answers, e.g. that the anisotropy parameter β for the photoionization of an *s*-like Dyson orbital is energy independent and equals 2 for linearly polarized light. Thus, the deviations from this behavior are due to the effects neglected in the model, i.e., interactions (exchange and correlation) of the ionized electron with the core and relativistic effects.⁷⁶ Calculations of β for Cl and Al that accounted for these effects^{77,79} revealed that anisotropic electron-ion interactions are non-negligible, whereas nonrelativistic effects were concluded to be less important.⁷⁶

Expressions for PADs for several special cases (e.g. diatomic molecules) taking into account rotational states have been developed and applied to interpret resonance enhanced multiphoton ionization (REMPI) and velocity map imaging measurements^{80–84} by fitting the dipole matrix elements and phases to match the experimental PADs.

Reed *et al.*,⁵⁴ who extended the central-potential model to molecular ions, reported encouraging results for threshold behavior of total cross sections. Their model employed plane-wave description of the ejected electrons and neglected ion-core interactions. Since their calculations relied on empirical Dyson orbitals (i.e., Slater functions with the exponents fitted to reproduce the experiment), it is difficult to assess the errors of the model due to the approximations in the description of the ejected electron and the accuracy of the model for the absolute values of the cross sections. The primary goal of the present work is to benchmark this approach by combining simple description of the photoelectrons with accurate *ab initio* Dyson orbitals.

Stehman and Woo introduced the zero-core-contribution (ZCC) model,⁸⁵ which also relies on a plane-wave description of the free electron and employs empirical representation of the atomic Dyson orbital. A ZCC calculation requires three parameters: angular momentum of the Dyson orbital, its average size, and IE. They reported absolute cross sections of photodetachment to be accurate to a factor of 2.

Several groups have been developing methodology that allows one to account for anisotropic interactions between the core and the ionized electron.^{86–89} For example, Lucchese *et al.* computed final-state wave continuum function using iterative Schwinger variational method and employing frozen Hartree–Fock representation of the core and single-center expansion technique.⁸⁶ Powis developed an effective potential model for the core.⁸⁷

The structure of the paper is as follows. In Sec. II we discuss the theoretical aspects of cross section calculations (Sec. II A), the treatment of the photoelectron wave function and the relation of differential cross sections to the quantity measured experimentally, and the β anisotropy parameter (Sec. II B). The details of the electronic structure and cross sections calculations are described in Sec. III. In Sec. IV, we first analyze the effect of the Dyson orbitals asymptotic behavior on the photoelectron dipole moments (Sec. IV A). Then we compare the performance of our model to the experimentally measured total cross sections (Sec. IV B) and photoelectron anisotropies (Sec. IV C). Our concluding remarks are given in Sec. V. Details about the isotropic averaging procedure are provided in the Appendix.

II. THEORY

A. Differential and total cross sections and Dyson orbitals

In the dipole approximation, the differential cross section for ionizing or detaching a photoelectron in the solid angle $d\Omega_k = \sin\theta d\theta d\phi$ is (in atomic units)⁹⁰

$$\frac{d\sigma}{d\Omega_k} = \frac{4\pi^2}{c} E |D_k^{IF}(\theta, \phi)|^2, \quad (3)$$

where E is energy of the ionizing radiation, \mathbf{k} denotes both energy and the direction of the ejected electron, and D^{IF} is the photoelectron matrix element connecting the initial and the final wave functions, see Eq. (1), which depends on the Dyson orbital and the wave function of the ionized electron. These equations are derived within sudden ionization approximation^{91,92} and strong orthogonality condition,^{14,17} i.e., assuming that ionization is fast and that the final state can be described by the noninteracting and orthogonal $N-1$ electron core and the continuum electron wave functions, $\Psi_F^{N-1}(1, \dots, n-1)$ and $\Psi_k^{\text{el}}(n, \sigma)$, respectively, with no correlation between the outgoing and the remaining $N-1$ bound electrons. Both approximations are usually justified by a small size of the core relative to the free electron wave function and, consequently, their vanishing overlap.^{14,17}

For molecular systems, where dipole matrix elements should also include vibrational wave functions of the initial and final states, Eq. (3) becomes

$$\frac{d\sigma}{d\Omega_k} = \frac{4\pi^2}{c} E \sum_{nn'} P_n |D_{nn'}|_{nn'}|^2, \quad (4)$$

where n and n' denote the initial and final vibrational levels, P_n gives the populations of the vibrational states of the initial system, and the energy of the ejected electron $E_{\text{el}}(k)$ satisfy the following energy balance:

$$E = \text{IE}_{00} + E_{\text{el}}(k) + E_{\text{vib}}^f(n') - E_{\text{vib}}^i(n), \quad (5)$$

where IE_{00} is adiabatic ionization/detachment energy of the ion, and $E_{\text{vib}}^{i,f}$ denotes vibrational energies of the initial and final system. IE_{00} is equal to EA of the neutral. The dipole matrix element $D_{nn'}|_{nn'}$ includes contributions from the electronic and vibrational, $\xi_n^i(R)$ and $\xi_n^f(R)$, wave functions:

$$D_{nn'}|_{nn'} = \int dR (D_k^{IF}(R) \xi_n^i(R) \xi_n^f(R)), \quad (6)$$

where R denotes nuclear coordinates. Within Condon approximation, the dependence of the electronic dipole matrix element on nuclear coordinates can be neglected:

$$D_k^{IF}(R) \approx D_k^{IF}(R_0), \quad (7)$$

$$|D_{nn'}|_{nn'}|^2 = |D_k^{IF}(R_0)|^2 FCF(n, n'), \quad (8)$$

$$FCF(n, n') = \left| \int dR \xi_n^i(R) \xi_n^f(R) \right|^2, \quad (9)$$

where R_0 denotes the equilibrium geometry of the initial electronic state.

Equation (3) gives the cross section for a molecule at given orientation, and one needs to average over all molecular orientations sampled in a particular experiment:

$$\frac{d\sigma}{d\Omega_k} = \frac{4\pi^2}{c} E \int d\alpha d\beta d\gamma |D_{nn'}^{IF}|^2 P(\alpha\beta\gamma) = \frac{4\pi^2}{c} E \overline{|D_{nn'}^{IF}|^2}, \quad (10)$$

where Euler angles $\{\alpha, \beta, \gamma\}$ specify molecular orientation, and $P(\alpha\beta\gamma)$ is a weighting function determined by the experiment, e.g., $P(\alpha\beta\gamma)=1$ for a single photon photodetachment, $\cos^2(\beta)$ or $\sin^2(\beta)$ in two-photon REMPI, etc. Finally, the total cross section is obtained from Eq. (3) by averaging over all orientations of the photoelectrons and laser polarization directions:⁵⁴

$$\sigma = \frac{8\pi^2}{3c} E \int d\Omega_k \overline{|D_k^{IF}|^2} = \frac{8\pi^2}{3c} E \int \sin\theta d\theta d\phi \overline{|D^{IF}(\theta, \phi)|^2}. \quad (11)$$

B. Plane wave description of the ejected electrons

In this work, we employ a simple plane wave description of photoelectrons, as in Ref. 54, to benchmark the performance of this model for photodetachment from negative ions. Plane waves are the exact eigenstates of the free electron in the absence of the interaction between the molecular core and the detached electron:

$$\Psi_k^{\text{el}} = |k\rangle = \sqrt{\frac{k}{(2\pi)^3}} e^{ikr}, \quad (12)$$

where the recommended⁹⁰ normalization per unit energy is employed. Neglect of the interaction is justified by a small size of the remaining core relative to the continuous states of the electron. Moreover, in the photodetachment from negative ions, the remaining core is neutral and therefore does not give rise to a long-range Coulomb potential.

To impose strong orthogonality condition,^{14,17} plane waves can be made orthogonal to the Dyson orbital by means of Schmidt orthogonalization, as has been done, for example, in Ref. 54:

$$|k'\rangle = |k\rangle - \langle\phi^d|k\rangle|\phi^d\rangle. \quad (13)$$

Such orthogonalization has shown to be important to reproduce correct threshold behavior of the cross sections. However, an identical result can be achieved by simply placing the centroid of the Dyson orbital in the zero of the laboratory frame,^{26,54} as done in the present work:

$$D^{IF} = \langle\phi^d|r|k'\rangle = \langle\phi^d|r|k\rangle - \langle\phi^d|k\rangle\langle\phi^d|r|\phi^d\rangle = \langle\phi^d|r|k\rangle. \quad (14)$$

The term $\langle\phi^d|r|\phi^d\rangle$ is zero due to our choice of the zero of the coordinate system, Eq. (40) in Ref. 26.

For deriving angular dependence (given by vector \hat{k}) of the dipole matrix elements D_k^{IF} , it is convenient to express plane waves in the basis of spherical waves $|E, l, m\rangle$:⁹³

$$|k\rangle = \sum_{l=0}^{\infty} \sum_{m=-l}^l |E, l, m\rangle \frac{1}{\sqrt{k}} Y_{lm}(\hat{k}), \quad (15)$$

$$|E, l, m\rangle = i^l \sqrt{\frac{2k}{\pi}} j_l(kr) Y_{lm}(\mathbf{r}), \quad (16)$$

where Y_{lm} and j_l are the spherical harmonics and spherical Bessel functions, respectively.

Substituting the above expansion into Eq. (1), we arrive:

$$\begin{aligned} |D_k^{IF}|^2 &= \sum_{l,l'=0}^{\infty} \sum_{m=-l}^l \sum_{m'=-l'}^{l'} \langle \phi_R^d | r_u | E, l, m \rangle \\ &\quad \times \langle E, l', m' | r_u | \phi_L^d \rangle Y_{lm}(\hat{k}) Y_{l'm'}^*(\hat{k}) \\ &= \frac{1}{2\pi k} \sum_{l,l'=0}^{\infty} \sum_{m=-l}^l \sum_{m'=-l'}^{l'} C_{kl'm'}^R \cdot (C_{klm}^L)^* Y_{lm}(\hat{k}) Y_{l'm'}^*(\hat{k}), \end{aligned} \quad (17)$$

$$= \frac{1}{2\pi k} \sum_{l,l'=0}^{\infty} \sum_{m=-l}^l \sum_{m'=-l'}^{l'} C_{kl'm'}^R \cdot (C_{klm}^L)^* Y_{lm}(\hat{k}) Y_{l'm'}^*(\hat{k}), \quad (18)$$

where ϕ_R^d and ϕ_L^d denote left and right Dyson orbitals, as defined in Ref. 26 (they are not identical owing to a non-Hermitian nature of EOM-CC), and the coefficients $C_{klm}^{R,L}$ are:

$$C_{klm}^{R,L} = 2ki^l \int \phi_{R,L}^d(\mathbf{r}) r_u j_l(kr) Y_{lm}(\theta, \phi) d\mathbf{r}. \quad (19)$$

We calculate coefficients $|C_{klm}^{R,L}|$ and/or their averaged values, $|\overline{C_{klm}^{R,L}}|$, by the numerical integration on the grid (see Appendix and Ref. 26). By integrating over ϕ , we arrive at the following expression for the cross section:

$$\begin{aligned} \frac{d\sigma}{\sin \theta d\theta} &= \frac{4\pi^2}{c} E \frac{1}{2\pi k^2} \sum_{ll'} \sum_{m=-\min(l,l')}^{\min(l,l')} \overline{|C_{klm}^R (C_{kl'm}^L)^*|} \\ &\quad \cdot \Theta_{lm}(\theta) \cdot \Theta_{l'm}(\theta). \end{aligned} \quad (20)$$

Equations (11) and (20) can be used for calculating total and differential cross sections, respectively. Finally, for the

incoming-wave boundary condition,⁹⁴ the phase factor in Eq. (19) becomes i^{-l} .

In the case of one-photon photodetachment using linearly polarized light, the differential cross section has the following form:⁹⁵

$$\frac{d\sigma}{\sin \theta d\theta} = \frac{\sigma}{4\pi} [1 + \beta P_2(\cos(\theta))], \quad (21)$$

where $P_2(\cos(\theta))$ is the second-order Legendre polynomial, and β is the so-called anisotropy parameter, a single quantity sufficient to characterize angular distribution of photoelectrons for a single-photon ionization. It assumes values from -1 for purely perpendicular transition to $+2$ for purely parallel transition. For these experiments, β can be extracted from Eq. (20) by fitting the computed $d\sigma/\sin \theta d\theta$ to Eq. (21). More efficiently, both σ and β can be computed from the values of $d\sigma/\sin \theta d\theta$ at $\theta=0$ and $\theta=\pi/2$, i.e., σ_{par} and σ_{perp} :

$$\sigma = \frac{4\pi}{3} (\sigma_{\text{par}} + 2\sigma_{\text{perp}}), \quad (22)$$

$$\beta = \frac{2(\sigma_{\text{par}} - \sigma_{\text{perp}})}{\sigma_{\text{par}} + 2\sigma_{\text{perp}}}. \quad (23)$$

C. A relationship of the present approach to the Cooper–Zare model

The physical assumptions behind our approach are identical to those used to derive the Cooper–Zare expression^{75,78} for anisotropy parameter β for the atomic ionization using linearly polarized light. For the atomic ionizations all angular averaging can be done analytically, and the resulting anisotropy parameter depends only on the radial one-electron dipole integrals. For the ionization from the atomic Dyson orbital with angular momentum l (e.g., $l=s, p, d, \dots$), β depends only on the relative cross sections of $l-1$ and $l+1$ partial waves and their relative phase:

$$\beta = \frac{l(l-1)\sigma_{l-1}^2 + (l+1)(l+2)\sigma_{l+1}^2 - 6l(l+1)\sigma_{l-1}\sigma_{l+1} \cos(\delta_{l+1} - \delta_{l-1})}{(2l+1)[l\sigma_{l-1}^2 + (l+1)\sigma_{l+1}^2]}, \quad (24)$$

where the cross sections $\sigma_{l\pm 1}$ are radial dipole matrix elements:

$$\sigma_{l\pm 1} = \int_0^\infty dr [\phi^d(r) r R_{kl}(r)]. \quad (25)$$

In many applications of the Cooper-Zare expression, these cross sections are evaluated using approximate atomic-like orbitals. However, these integrals can be easily computed using our Dyson orbitals and the radial functions from Eq. (16). Thus, for the atomic photodetachment, the results of

our calculations using numeric angular averaging are identical to the calculations using Eq. (24) with the numerically computed radial dipole integrals and setting the phase shift to zero.

This provides a useful tool for validating the accuracy of the angular averaging, as well as allows us to investigate the effects of nonzero phase shift on β . Similar computations can be performed for simple diatomics whose Dyson orbitals resemble atomic orbitals. For example, the π^* -like Dyson orbital corresponding to photodetachment from O_2^- or S_2^- is almost identical to an atomic d -orbital, which has been ex-

ploited in interpreting the experimental measurements.^{96,97} The differences between Cooper–Zare and full spherical averaging using our code can be used to assess the validity and limits of such approach.

Equation (24) sets boundaries to the possible values of β , as well as its energy dependence. We can determine boundaries for β for molecular photodetachment by varying the phase factors in our model. If the experimental results fall outside of these boundaries, it would mean that either Dyson orbitals are not sufficiently accurate, or that the interactions between the core and the ionized electron are not negligible.

In the rest of this subsection, we consider photodetachment from a p -orbital. We use this example to check our expressions for consistency and to analyze the relationship between the present approach and the Cooper–Zare model. In the case of p -atom, the only final states are s - and d -waves. The Cooper–Zare anisotropy parameter is then:

$$\beta = \frac{2(\sigma_d^2 - 2\sigma_s\sigma_d \cos \delta)}{\sigma_s^2 + 2\sigma_d^2}. \quad (26)$$

The calculations using Eq. (20) can be set up in several ways. First, the state degeneracy can be dealt with differently. One can start with a randomly oriented p -orbital and perform isotropic averaging (as one would do in a molecular case). Alternatively, the differential cross section can be computed as the sum of cross sections computed for p_x , p_y , and p_z orbitals. This allows us to verify that the numerical averaging over the orientations is performed properly.

Choosing the latter approach, one can derive analytic total cross section and β by using Eqs. (22) and (23). For the z -polarized light, p_z orbital yields s -wave (C_{00}) and d_z^2 (C_{20}), whereas p_x and p_y yield equal mixtures of d_{2-1} and d_{2+1} (C_{2-1} and C_{2+1}). Thus, only the p_z orbital contributes to σ_{par} and σ_{perp} :

$$\sigma = N(C_{00}^2 + \frac{5}{2}C_{20}^2), \quad (27)$$

$$\beta = \frac{2(\frac{5}{4}C_{20}^2 - \sqrt{5}C_{00}C_{20})}{C_{00}^2 + \frac{5}{2}C_{20}^2}, \quad (28)$$

where N denotes the prefactor in Eq. (20). Alternatively, σ can be computed from Eq. (20) as follows:

$$\sigma = N(C_{00}^2 + C_{20}^2 + C_{2-1}^2 + C_{2+1}^2). \quad (29)$$

In order for the two cross sections to agree, the following relationship needs to be satisfied:

$$\frac{5}{2}C_{20}^2 = C_{20}^2 + C_{2+1}^2 + C_{2-1}^2, \quad (30)$$

which means that

$$C_{2\pm 1}^2 = \frac{3}{4}C_{20}^2. \quad (31)$$

This relationship indeed holds, as can be verified analytically by considering angular dependence of the respective integrals, as well as numerically, by comparing the values of the computed coefficients.

By comparing β in Eqs. (28) and (26), we arrive at

$$\sigma_s = C_{00}, \quad (32)$$

$$\sigma_d = \frac{\sqrt{5}}{2}C_{20}. \quad (33)$$

Alternatively, by separating the angular dependence of the Dyson orbital and performing integration over angular variables in Eq. (19), we obtain

$$\frac{C_{00}}{C_{20}} = \frac{2}{\sqrt{5}} \frac{\sigma_s}{\sigma_d}. \quad (34)$$

Thus, our expression for angular distribution is fully consistent with the Cooper–Zare expression.

III. COMPUTATIONAL DETAILS

The Dyson orbitals for photodetachment from atomic and molecular anions were computed using the EOM-CCSD suite of methods implemented in the Q-CHEM electronic structure package.⁹⁸ Most of the anions in this study have well-behaved ground state wave functions, i.e. closed-shell singlets (H^- , Li^- , F^- , NH_2^- , OH^-) or high-spin triplets (C^-). The initial and final states of these systems were described by CCSD and EOM-IP-CCSD, respectively, employing Hartree–Fock reference corresponding to their ground states.

For O^- , O_2^- , and S_2^- , we employed a high-spin triplet state of the corresponding neutral species as the reference. With this reference, the anions states were computed by EOM-EA/SF-CCSD, and the states of the neutrals by EOM-SF-CCSD.

Dyson orbitals of the molecular anions were computed at the anions equilibrium geometries optimized at the CCSD(T)/aug-cc-pVTZ level using the MOLPRO quantum chemistry package.⁹⁹ The optimized geometry parameters are: $r_{\text{OO}}=1.228$ Å (O_2^-), $r_{\text{OH}}=0.968$ Å (OH^-), $r_{\text{NH}}=1.031$ Å, $\angle_{\text{HNH}}=101.8^\circ$ (NH_2^-), and $r_{\text{SS}}=1.936$ Å (S_2^-).

We found that the computed cross sections are more sensitive to the one-electron basis set than energy differences, and a large number of diffuse functions is required for converged cross sections, as demonstrated below. For example, while the addition of several sets of s and p diffuse Gaussians results in small changes in the electronic state energies (i.e., 10^{-2} eV), the respective changes in the Dyson orbitals yield noticeable differences (up to 15%) in the resulting cross sections.

We employed several types of Pople,^{100,101} 6-311G($n+$) \times (mdf, mpd) with $n=1-7$, $m=1-3$, and Dunning¹⁰² bases. For the Pople basis sets,^{100,101} adding more polarization functions beyond $2d(2p)$ resulted in small changes in the cross sections (under 5%), however, for the benchmark purposes we employed larger $3df(3pd)$ bases. To compare the performance of the Pople and Dunning basis sets, the following modified bases were also considered: cc-pVTZ($n+$), aug-cc-pVTZ($n+$), and aug-cc-pVTZ+ $nsnp$. The cc-pVTZ($n+$) sets were constructed from cc-pVTZ by adding the same (sp) diffuse sets as in the corresponding Pople bases. The aug-cc-pVTZ($n+$) bases are derived in a similar way from aug-cc-pVTZ: The original set of s , p , d , and f diffuse Gaussians from aug-cc-pVTZ is kept, and the second and higher (sp) diffuse sets were taken from Pople bases. For aug-cc-pVTZ+ $nsnp$, the original Dunning set was aug-

mented by more diffuse s and p Gaussians with the exponents obtained by successively dividing the lowest exponent by two.¹⁰³

These Dyson orbitals were used as input for the EZDYSON program^{26,104} for cross section calculations. First, electronic dipole matrix elements $D_k^{IF}(R_0)$ are computed using Eq. (1) and averaged over molecular orientation $\{\alpha\beta\gamma\}$, as required by Eq. (10). For atoms, no averaging is necessary, but the contributions from different atomic states (e.g., p_x , p_y , and p_z) need to be summed up. At each Euler point, the orbital is rotated to the lab frame and matrix element (1) is computed by numeric integration over a Cartesian $\{xyz\}$ grid in the laboratory frame. Convergence with respect to the density of the Cartesian grid is achieved quite readily. The cutoff size of the $\{xyz\}$ box was determined by the radius at which the long-range Dyson orbital oscillations begin (see the next section), or, when there are no oscillations, at the radius when the amplitude becomes smaller than 10^{-7} . The number of points along each $\{xyz\}$ axis are listed in the supplementary material.¹⁰⁵ The density of the angular Euler grid, which is limited by computational cost considerations, can introduce small numerical errors. We employed $18 \times 10 \times 18$ $\{\alpha\beta\gamma\}$ grid, i.e., 20° rotations around each axis. We estimate the numerical errors in the cross sections due to this grid are around 5%. For example, isotropic averaging for p -orbital photodetachment gives slightly different values for parallel or perpendicular ionization light polarization (e.g., p_x versus p_z) in the initial orientation, $\alpha=\beta=\gamma=0^\circ$. For example, the cross section for ionization from an isotropically averaged p_x orbital (exponent $\alpha=1.0$ a.u.) is 6.33×10^{-4} bohr⁻², assuming the electron binding energy of 1.0 and 0.01 eV electron kinetic energy. The same cross section for a isotropically averaged p_z orbital is 6.71×10^{-4} bohr⁻². For a 1.0 eV photoelectron, the cross sections are 1.18×10^{-2} and , respectively. p_x results are closer to the exact value, so the parallel orientation was used as the starting point in all calculations, while the perpendicular results were checked in a few cases. The integration over an isotropic ensemble of orientations in the lab frame is described in the Appendix.

Once averaged electronic dipole moment matrix elements $|D_k^{IF}|$ are computed, the cross sections $\sigma(E)$ are calculated as follows. For atomic systems, $\sigma(E)$ are given by Eq. (11), with k satisfying the following energy balance:

$$\frac{k^2}{2} = E - \text{IE}. \quad (35)$$

For molecular anions, $FCF(n, n')$ [see Eq. (9)] were computed using double-harmonic parallel normal mode approximation by the EZSPECTRUM program.¹⁰⁶ Assuming vibrationally cold anions ($P_n = \delta_{n0}$), the cross sections are computed as follows:

$$\sigma = \frac{2}{3} \frac{4\pi^2}{c} E \sum_{n'} \int \sin \theta d\theta d\phi |D_k(\theta, \phi)|^2 FCF(0, n'), \quad (36)$$

where k depends on E , IE, and n' via:

TABLE I. EAs (eV) used in the calculations.

Anion	EA	Reference
F	3.400	116, 117
C	1.260	118
O	1.460	119
H	0.754	120, 121
Li	0.618	111, 112
OH	1.83	122
O ₂	0.446	123
NH ₂	0.744	124

$$\frac{k^2}{2} = E - \text{IE}_{00} - E_{\text{vib}}^f(n'). \quad (37)$$

Finally, we arrive at

$$\sigma = \frac{2}{3} \frac{4\pi^2}{c} E |D_k|^2 \int_{\text{IE}_{00}}^{\text{IE}_{0n}} FCF(0, n) dE, \quad (38)$$

$$\frac{k^2}{2} = E - \text{IE}_{00}. \quad (39)$$

The EAs (IE_{00}) used in the cross sections calculations are given in Table I. For the molecular anions, we assume that the total energy of the ionizing radiation is the sum of EA, the kinetic energy of the photoelectron, and the change in vibrational energy, with no energy being transferred to rotations.

IV. RESULTS AND DISCUSSION

A. Asymptotic behavior of the Dyson orbitals and their basis set dependence

Photodetachment cross sections $\sigma(E)$ and anisotropy parameters β depend strongly on the basis set used to calculate the corresponding Dyson orbitals. For example, the addition of more than two sets of diffuse functions changes EOM-CCSD energies by about 10^{-2} eV, however, resulting small changes in the Dyson orbital yield significant variations in the calculated cross section and the anisotropy parameter. This suggests that the shape of the tail of the Dyson orbital plays an important role.

Below we discuss the origin of this behavior using F^-/F example for which we observed most severe basis set dependence. Since F^- is a closed-shell singlet, possible orbital artifacts due to spin contamination can be ruled out.

Figure 1 shows the one dimensional profile of the F^-/F Dyson orbitals computed using different Pople bases with an increasing number of diffuse functions. In the 0–4 Å valence region (Fig. 1, top), the shapes of the orbitals are similar. However, they become significantly different beyond 5 Å (Fig. 1, bottom). Zooming in the tail region, we observe significant changes in the spatial extent of the orbital upon adding a second set of diffuse functions. However, the larger 6-311G(n)(3df) bases ($n=3-5$) do not result in extended electron density relative to 6-311G(2+)(3df), but exhibit

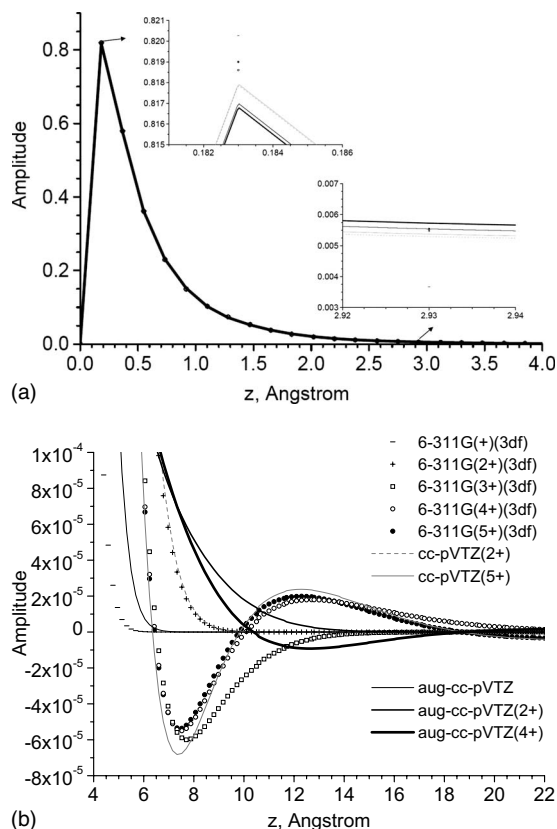


FIG. 1. Dyson orbitals profiles for F^- photodetachment obtained using different basis sets in the valence region (upper panel) and at large radii. Inserts show the regions around the indicated points zoomed in.

an oscillatory behavior beyond approximately 6.5 Å. The overall shape of Dyson orbitals converges only at the 6-311G(5+)(3df) level.

The correct asymptotic behavior of electronic density is described by exponential decay, which suggests that these long-range oscillations are numerical artifacts. Similar conclusions have been drawn by Chan and co-workers, who investigated nodal behavior of Hartree–Fock (HF) wave functions¹⁰⁷ and also observed unphysical long-range nodes. To determine the source of these oscillations, we analyzed the underlying HF MOs constituting the 6-311G(5+)(3df) Dyson orbital, as shown in Fig. 2. The largest contribution comes from the p_z occupied MO, ϕ_3 , which is very similar to the Dyson orbital, with small contributions from virtual p_z -like HF orbitals. Both the occupied and unoccupied HF orbitals exhibit oscillatory behavior at larger radii, which indicates that these oscillations are not due to the inclusion of correlation. Concurring with the conclusions of Ref. 107, we believe that with increasing basis set size, the HF procedure tries to optimize the shape of the MOs in the valence region, which has the strongest effect on the energy, whereas the behavior in the asymptotic region has negligible effect on the total energy, and, therefore the shape of the orbitals far from the nucleus is pretty much random. Thus, Dyson orbitals for photodetachment from negative ions are one of the cases when the incorrect asymptotic behavior of Gaussian versus Slater orbitals becomes important.

It is interesting that the occupied p_z MO obtained from OO-CCD calculations¹⁰⁸ is even closer to the Dyson orbital

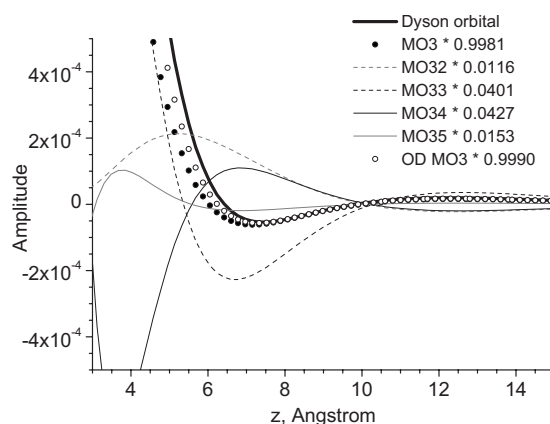


FIG. 2. Dyson orbital profile for F^- photodetachment calculated using 6-311G(5+)(3df) basis set and its decomposition in the leading HF orbitals. MOs are scaled by the coefficient they have in the right Dyson orbital. Also shown, the occupied MO with the major contribution obtained by OO-CCD calculation.

than the corresponding leading HF orbital, ϕ_3 . This confirms the observation of Ortiz²² that Bruckner orbitals are more suitable for Koopmans' model of ionization as they include orbital relaxation and correlation effects.

The performance of the Dunning basis sets was also investigated. To separate the effects of the valence and diffuse functions, we employed the cc-pVTZ basis augmented by the same (sp) diffuse sets from the Pople bases, e.g., cc-pVTZ($n+$), $n=1-4$. As seen in Fig. 1, these orbitals are very similar to the corresponding 6-311G($n+$)(3df) ones. However, the bases starting from aug-cc-pVTZ to which we add only the second and higher order Pople (sp) diffuse sets [i.e., aug-cc-pVTZ($n+$)] exhibit a much better asymptotic behavior. The aug-cc-pVTZ(2+) orbital, which is similar in quality to the 6-311G(3+)(3df) one, has a smooth monotonic decrease in the asymptotic region, while aug-cc-pVTZ(3+) and (4+) have smaller oscillations (10^{-6} versus 10^{-5} amplitude), starting at larger radii with respect to the corresponding Pople bases. The difference between the aug-cc-pVTZ($(n-1)+$) and cc-pVTZ($n+$) consists just in the first diffuse s and p functions, while the augmented d and f Gaussians do not contribute to ϕ^d .

Dyson orbitals for C^- and O^- photodetachment exhibit similar basis set effects. The effect of these long-range small-amplitude oscillations on the cross sections is significant because of the dipole moment operator which amplifies the long-range contributions. Figure 3 shows the profile of Dyson orbitals multiplied by z to illustrate the effect of multiplication by r in Eq. (1). Figure 3 also demonstrates the relative sizes of the atomic anions. Note that the amplitude of the tail oscillations decreases as the atomic radius increases, e.g., the basis set dependence is the strongest for F^- . This is because in the case of more electronegative atoms the valence orbitals are tighter and the optimization is skewed even more towards short distances. Dyson orbitals for H^- and Li^- photodetachment (not shown) have tails that extend to very large radii (25–40 Å), with very small oscillations (10^{-7} amplitude) only at the largest bases 6-311G($n+$)(3pd), $n=4-5$.

In summary, our examination of the asymptotic behavior and basis set dependence of Dyson orbitals shows that the

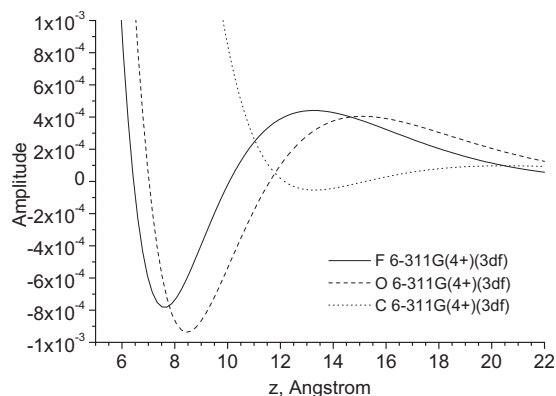


FIG. 3. Dyson orbitals multiplied by z , $z \cdot \Phi^d(0,0,z)$ for F^- , O^- , and C^- photodetachment calculated using 6-311G(4+)(3df) basis sets.

aug-cc-pVTZ($n+$) bases are more suitable for calculations of photodetachment from negative ions. However, as Ref. 107 demonstrated, none of the Gaussian-type bases is free from unphysical long-range behavior. Thus, we simply cut off unphysical oscillations (both in Pople and Dunning bases) when performing numerical integration in the $\{xyz\}$ lab frame by using integration box with a carefully selected size corresponding to the radius where a Dyson orbital starts oscillating. Although this solution is not fully satisfactory, it removes the artifacts in $\sigma(E)$ and $\beta(E)$ due to the long-range oscillations. For the cases where Dyson orbital oscillations are small, aug-cc-pVTZ($n+$) or larger anions like C^- , no cut-offs are necessary, however, we used them for consistency.

To conclude, the strong effect of the asymptotic orbital behavior on $\sigma(E)$ and $\beta(E)$ can be rationalized as follows. First, increasing the basis results in larger Dyson orbital changes in the valence region (10^{-3} differences in amplitudes, see Fig. 1) and much smaller ones at large radii (10^{-4} – 10^{-5}). Even though these oscillations are small compared to the electronic density in the valence region, they are amplified by multiplication of r in the dipole matrix element calculation, see Eq. (1) and Fig. 3, and by the fact that the spherical waves with higher angular momentum l have maximum density at larger radii. These oscillations result in artifacts in $\sigma(E)$ and unphysical $\beta(E)$ curves, especially at lower photoelectron kinetic energies, as explained below. The anisotropy parameter is particularly sensitive to the ratio of the radial dipole matrix elements [Eqs. (24) and (25)]. The spherical Bessel functions display tighter oscillations with increasing energy, such that low energy waves have considerable density in the asymptotic region of the Dyson orbitals.

B. Total photodetachment cross sections

In this section we benchmark our model against the experimental data for photodetachment cross sections for atomic and small molecular anions. Basis set effects, which are found to be significant, are examined in detail for the F^- and C^- anions. As noted before,⁵⁴ the cross section dependence on energy for photodetachment from p orbitals is characterized by a rapid increase near the threshold which levels off at higher energies.

Figure 4 (top) shows the total cross section for F^- as a

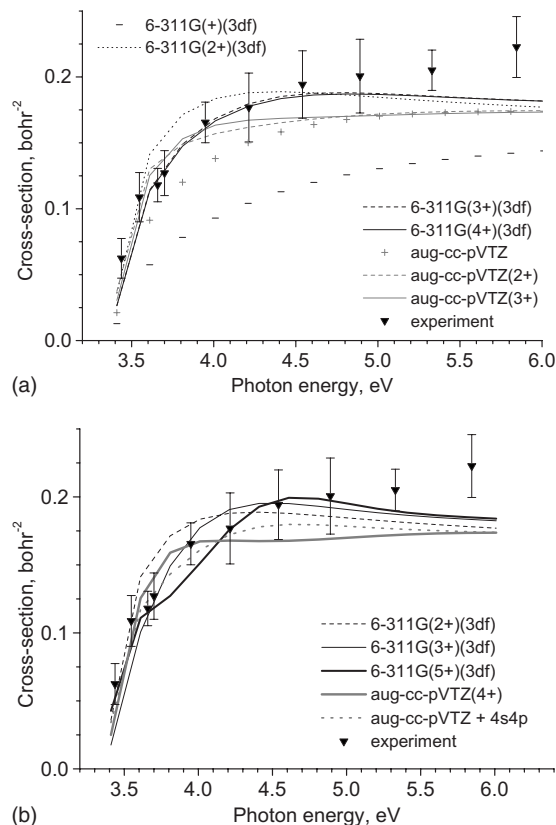


FIG. 4. Absolute photodetachment cross sections for F^- photodetachment calculated using different basis sets with (upper panel) and without (lower panel) cutoffs (see text). Experimental data and error bars from Ref. 125.

function of ionizing radiation energy computed with several 6-311G($n+$)(3df) bases with an increasing number of the diffuse (sp) sets and with the appropriate cutoffs of the ϕ^d . Whereas $n=1$ is clearly insufficient, $n=2$ results are already fairly close to the experimental values. However, complete convergence is achieved only with 6-311G(3+)(3df).

The cross section values obtained using the aug-cc-pVTZ basis are in between the $n=1$ and $n=2$ curves, as expected from the behavior of the corresponding Dyson orbitals in Fig. 1. Total cross sections calculated with an increasing number of (sp) diffuse functions added to aug-cc-pVTZ show similar convergence, but the calculated values are in slightly worse agreement with respect to the experimental data points than the converged Pople basis results.

The $\sigma(E)$ curves obtained without the cutoff of Dyson orbital oscillations converge only at the 6-311G(5+)(3df) level (Fig. 4, bottom). This last curve also shows an unphysical kink at approximately 3.6 eV, reproduced by cc-pVTZ(5+) and 6-311G(4+) calculations, which is due to the oscillatory ϕ^d behavior beyond 6.5 Å.

Total cross sections for C^- photodetachment (Fig. 5) are converged with the 6-311G(2+)(3df) basis, and the results with or without cutoff are almost identical, due to the much smaller oscillations in ϕ^d at large radii. Total cross sections obtained using aug-cc-pVTZ($n+$) bases converge to slightly lower values, as in the F^-/F case. It is difficult to assess whether the Pople or the Dunning bases calculations are closer to the actual value, since experimental errors are on the same order or larger than the differences between them.

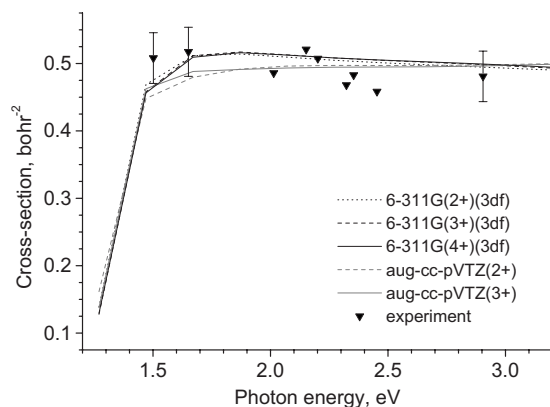


FIG. 5. Absolute photodetachment cross sections (C^-) calculated using different basis sets. Experimental data and error bars from Ref. 126.

The O^- photodetachment cross sections are plotted in Fig. 6. Two oxygen states are accessible within the range of ionizing radiation used in the experiments,^{109,110} the ground state 3P (above 1.46 eV) and the first excited state 1D (above 3.43 eV).¹¹⁰ Convergence of the calculated cross sections is achieved for the 6-311G(3+)(3df) basis. Unlike F^- and C^- results, the absolute values are about 2.6 times lower than the experimental ones. The overall shape of $\sigma(E)$ is correct and the scaled curve (using 1/0.38) matches the experiment. For the converged and scaled 6-311G(3+)(3df) values, the largest errors with respect to the experiment are around 30% in the threshold region and 25% for the excited state data.

In the case of photodetachment from s -orbitals, we consider the H^- and Li^- anions. Cross section for H^- (Fig. 7) converges at a larger basis, 6-311G(4+)(3pd), while for Li^- , even the 6-311G(+)(3df) curve is very close to the converged 6-311G(3+)(3pd) one (Fig. 8). The calculated values for H^- are in good agreement with the experiment, with maximum errors around 9% at the peak region. The $\sigma(E)$ curves for Li^- are slightly shifted on the energy axis and were scaled down by a factor of 1.21. It is interesting to notice that the experimental curve rises before the threshold energy value (0.618 eV).^{111,112} Similarly, the change in slope due to Li^- photodetachment to the first Li excited state appears earlier than the second threshold value of 2.5 eV.¹¹³ The fast drop of $\sigma(E)$ at the higher energies is also not reproduced by the calculations.

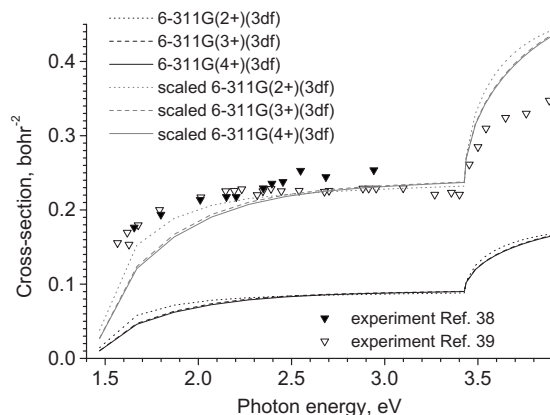


FIG. 6. Absolute photodetachment cross sections (O^-) calculated using different basis sets. Experimental data and error bars from Refs. 109 and 110.

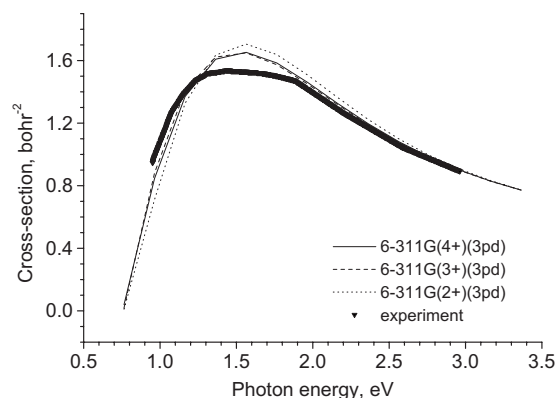


FIG. 7. Absolute photodetachment cross sections (H^-) calculated using different basis sets. Experimental data from Ref. 127.

To determine the performance of our method for larger, nonspherically symmetric systems, we computed the photodetachment cross sections for the NH_2^- , OH^- , and O_2^- molecular anions. NH_2^- and OH^- have p -shape Dyson orbitals (non-bonding lone-pair electrons at the heavy atom) and the $\sigma(E)$ curves resemble those for second row anions. Calculations for NH_2^- photodetachment (Fig. 9) are in very good agreement with the experiment, especially considering the large scattering of the experimental data points. The OH^- calculated $\sigma(E)$ curves (Fig. 10) were scaled up (by 1/0.85) and give better agreement with the experiment for smaller bases, similar to the O^- case. The FCFs are not important for NH_2^- and OH^- . In both cases, the changes in geometry are small giving rise to a single peak in FCF. In this case of diagonal transitions, the effect of FCFs on the cross section reduces to a scaling factor, which is negligible (0.999) for NH_2^- and OH^- .

O_2^- loses an electron from the π^* orbital, which has a d -like shape, and the behavior of the $\sigma(E)$ curve is different from the anions discussed above. Three electronic states of O_2 are accessible in the energy range shown in Fig. 11: $^3\Sigma_g^-$, $^1\Delta_g$, and $^1\Sigma_g^+$. The respective EAs are: 0.448, 1.4262, and 2.072 eV (see, for example, Ref. 97), while equilibrium distances and frequencies were taken from Ref. 55. The experimental curve was calibrated using O^- data, and the accuracy of 14% in the absolute values was reported in Ref. 114. At

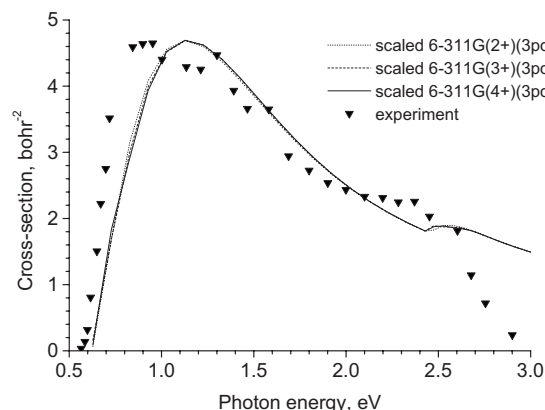


FIG. 8. Absolute photodetachment cross sections (Li^-) calculated using different basis sets. The calculated values are scaled down by a factor of 1.21. Experimental data from Ref. 113.

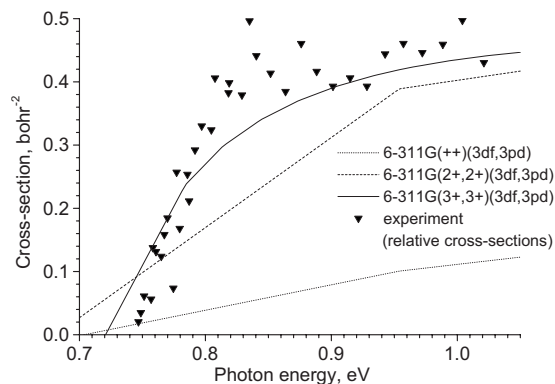


FIG. 9. Absolute photodetachment cross sections (NH_2^-) calculated using different basis sets. Experimental data from Ref. 124.

energies below 1.43 eV, when only the ground electronic state of O_2 is accessible, scaling the computed cross sections for ground state O_2 by factor of 2 gives good agreement with the experimental data (Fig. 11 top). Including FCFs in the calculation clearly improves the shape of $\sigma(E)$ curve. When all three (or two) states are taken into account, as necessary in the energy range between 1.43 and 2.07 eV (and above 2.07 eV) the resulting cross section curve rises too steeply. Absolute values vary from being up to a factor of 2 too low at lower energies to being too high (up to a factor of 2) at higher energies. The comparison of individual cross sections and FCFs (bottom panel of Fig. 11) shows that the cross sections for the singlet states rise much faster and are larger than that of the triplet state, while the integrated FCFs have similar behavior. The analysis of the corresponding Dyson orbitals reveals that the Dyson orbital for the triplet ground state of oxygen is more diffuse. This may be due to a more effective screening of the core in the ground state relative to the excited states.

C. Angular distributions of photoelectrons and anisotropy parameter

In this section we test our model by calculating β anisotropy parameters for photodetachment from p -type atomic anions and the O_2^- and S_2^- molecular anions. The calculation of anisotropies is very sensitive to the asymptotic behavior of the Dyson orbitals. For the second row atomic anions the

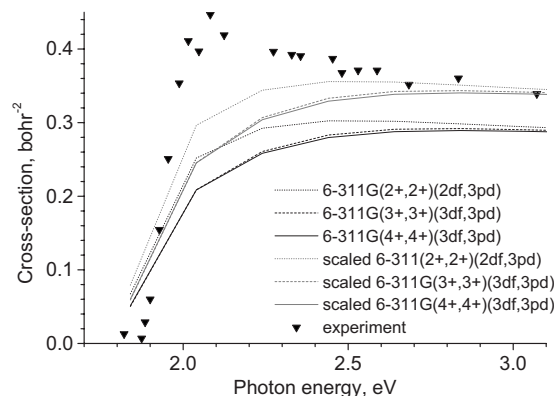


FIG. 10. Absolute photodetachment cross sections (OH^-) calculated using different basis sets. Experimental data from Ref. 122.

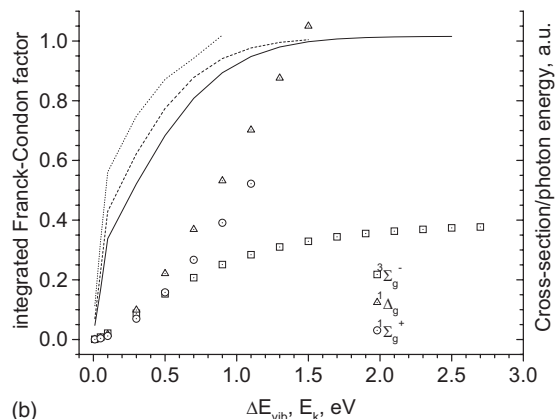
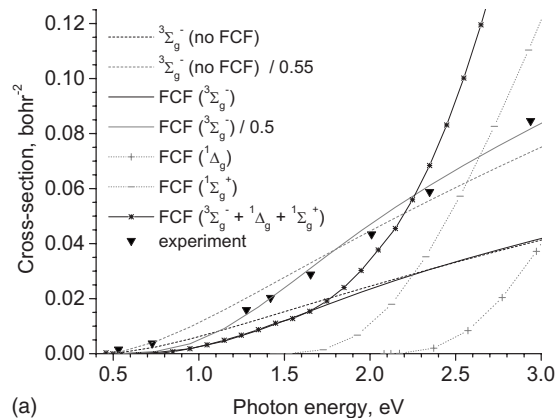


FIG. 11. Top: Absolute cross sections for O_2^- photodetachment calculated using 6-311G(2+)(3df) basis with or without taking into account FCFs. The individual curves for each electronic state of O_2 and their sum are shown. Experimental data from Ref. 114. Bottom: FCFs for each electronic state of O_2 as a function of vibrational energy ΔE_{vib} (the respective IE_{00} are set to zero). The corresponding absolute cross sections divided by the photon energy (and thus dependent only on electron kinetic energy) are shown on the same scale.

essential quantity that determines β at each energy is the ratio of the partial cross sections for the d and s spherical waves, see Eqs. (24) and (25). While absolute cross sections, Eq. (18), depend linearly on the errors in the partial cross sections for different l spherical waves, β depends nonlinearly on the σ_d/σ_s ratio, and is, therefore, more sensitive to the same errors in σ_d and σ_s . Thus, applying a cutoff radius for each Dyson orbital is essential. β calculations without the cutoffs give rise to a different slope for the $\beta(E)$ curves, with large, unphysical kinks at arbitrary energies.

The calculated and experimental anisotropy parameters for the p -type atomic anions are shown in Fig. 12. All $\beta(E)$ curves show an initial decrease in β as σ_d^2 and $\sigma_s\sigma_d$ in Eq. (26) increase with energy, followed by a turning point at which the sign of the slope changes. All computed curves are quite far from the experimental points, and the turning points appear at higher energies. This behavior suggests that the calculations underestimate the d -component. Figure 12 also reveals the effect of the anion size; the larger the anion (more diffuse Dyson orbital), the faster the increase in σ_d and the lower the energy for the turning point: $\text{Si}^- > \text{C}^- > \text{O}^- > \text{F}^-$. However, this effect is exaggerated in the calculated curves relative to the experimental data. Using different phase factors in Eq. (26) to account for the interference between s and

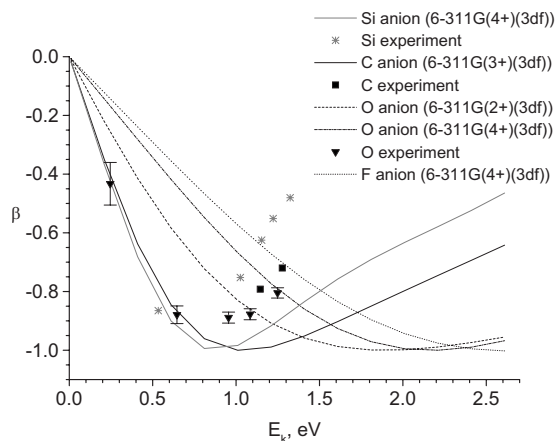


FIG. 12. Experimental and calculated anisotropy parameters for F^- , O^- (Ref. 128), C^- , and Si^- (Ref. 129).

d waves does not bring the calculated β closer to the experimental values. A $\cos \delta = 1$ in Eq. (26) gives rise to a maximum contribution from the perpendicular component $-\sigma_d \sigma_s$. For $\cos \delta < 1$, the initial $\beta(E)$ slope decreases and the turning point shifts to a less negative β , but stays at the same energy.

The only possible way to reproduce the experimental data within the present model is to consider a change in the σ_d/σ_s ratio, and below we quantify the difference between the computed and the “target” values. The gray curve in Fig. 13 (top) shows that for C^- increasing the σ_d^2/σ_s^2 ratio by a factor of 2.5 yields excellent agreement with the experiment. The same factor works for Si^- . For O^- the increase in the σ_d^2/σ_s^2 ratio necessary to fit the experimental data is quite large [Fig. 13, bottom panel], 5 for 6-311G(2+)(3df), and 9 for 6-311G(4+)(3df). In addition, a phase factor of 0.95 was necessary for a good fit with both bases. As for absolute cross sections calculations, 6-311G(2+)(3df) results are in better agreement with the experiment than the 6-311G(4+) \times (3df) ones.

Modifying the σ_d/σ_s ratio by a constant (i.e. energy-independent) factor is somewhat artificial since the correct ratio varies with energy. The incorrect asymptotic behavior (e.g., too fast decay due to using Gaussian-type bases) of the tail of the Dyson orbitals could be the source of the discrepancies. To test this assumption, we considered modified Dyson orbitals (for C^- photodetachment) in which we gradually increased the contribution of one of the diffuse Gaussians. That is, the coefficient for the Gaussian orbital with the exponent $\alpha = 1.319\,277 \times 10^{-2}$ a.u. was increased from approximately 0.05 in the actual left and right Dyson orbitals (6-311G(3+)(3df)) to 0.1, 0.15 and so on, while the other coefficients were kept the same. The resulting β are displayed in Fig. 13 (top). We observed that an increase from 0.05 to 0.1 results in very good agreement with the experimental curve. Figure 14 and Table II quantify the resulting changes in the Dyson orbital. The renormalized Dyson orbitals are plotted in Fig. 14. The target “0.1” Dyson orbital shows a change in the amplitude of approximately 10^{-2} and 10^{-3} at the peak and tail regions, respectively. As shown in Sec. IV A, the amplitudes of the Dyson orbitals calculated with different basis sets differ by approximately 10^{-3} . Thus,

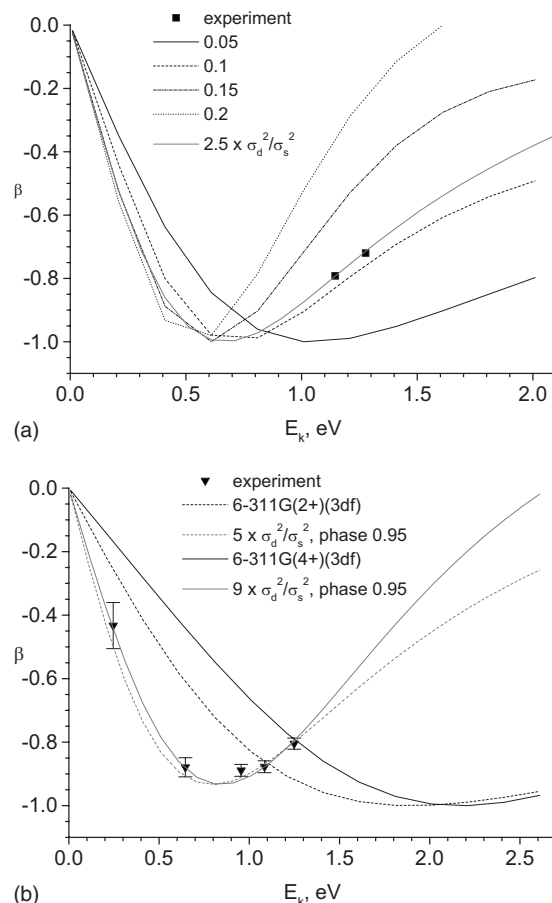


FIG. 13. The effect of increasing diffuse character and/or relative weight of the d -wave on the anisotropy parameter for C^- (top) and O^- (bottom) photodetachment. In the first case the coefficient of the diffuse Gaussian is shown, in the latter, the scaling and phase factors (see text).

a 10^{-2} change in the amplitude is likely to result in noticeable changes in energy. The average Z^2 value changes from 1.21 to 1.35 Å, and $\langle R^2 \rangle$, from 2.02 to 2.25 Å. Thus, this test suggests that our electronic structure calculations underestimate the amplitude of the Dyson orbitals in the tail region, which is likely to be source of differences with respect to the experimental data.

It is important to note that the above two approaches,

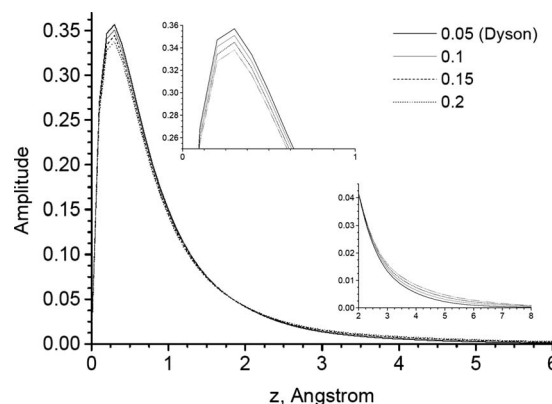


FIG. 14. Comparison of the orbitals derived from the computed Dyson orbital for C^- by increasing the coefficient of one of the diffuse basis functions (see text).

TABLE II. Properties of the modified Dyson orbital (C^-) calculated using the 6-311G(3+)(3*df*) basis with an increasing contribution from the diffuse Gaussian AO with the exponent $1.319\,277 \times 10^{-2}$.

Coefficient	Weight (norm=1) (%)	$\langle X^2 \rangle, \langle Y^2 \rangle$ (Å)	$\langle Z^2 \rangle$ (Å)	$\langle R^2 \rangle$ (Å)
0.05 (Dyson)	0.6	0.40	1.21	2.02
0.1	2.3	0.45	1.35	2.25
0.15	5	0.55	1.66	2.77
0.2	8.5	0.62	1.87	3.12

increasing the σ_d^2/σ_s^2 ratio by a constant factor and using more diffuse Dyson orbitals, are different conceptually as they yield constant versus energy dependent changes in the σ_d^2/σ_s^2 ratio. However, both approaches can reproduce the experimental anisotropies well. Therefore, more investigations are necessary in order to draw a clear conclusion on this issue.

In the case of molecular anion photodetachment, Dyson orbitals do not show any oscillatory behavior at large radii and calculations are less sensitive to the basis set size. We calculated $\beta(E)$ for the O_2^- and S_2^- anions.

Calculated and experimental $\beta(E)$ for O_2^- photodetachment are shown in Fig. 15. In the experiment using 780 nm wavelength (1.59 eV), only the ground electronic state of O_2 $^3\Sigma_g^-$ is accessible, with possibly some contribution from the $^1\Delta_g$ state at the lowest energy β point. The comparison of the experimental data with β computed for the $^3\Sigma_g^-$ state shows a trend similar to atomic anions: The computed anisotropy parameter decreases too slow relative to the experimental curves. At shorter wavelength (396 nm, 3.13 eV), all three states can contribute at electron kinetic energies (E_k) below 1.06 eV. Photoelectrons with E_k between 1.06 and 1.70 eV can originate from the $^3\Sigma_g^-$ and $^1\Delta_g$ transitions. At E_k higher than 1.70 eV the only accessible state is $^3\Sigma_g^-$, as in the 780 nm experiment, so the $\beta(E)$ curve for $^3\Sigma_g^-$ could be traced by following these data points obtained with different photon wavelengths. Also the observed angular distribution can be different for different wavelengths. However, we find that the shapes of the respective Dyson orbitals are very similar, the orbitals corresponding to the singlet target states being slightly less diffuse. Based on these orbitals, the com-

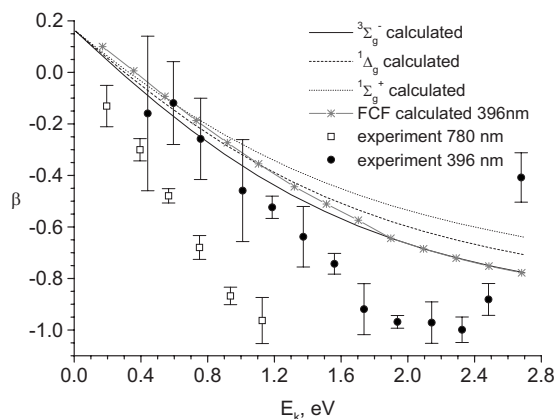


FIG. 15. Experimental (Ref. 97) and calculated (6-311G(2+)(3*df*)) anisotropy parameter for O_2^- photodetachment.

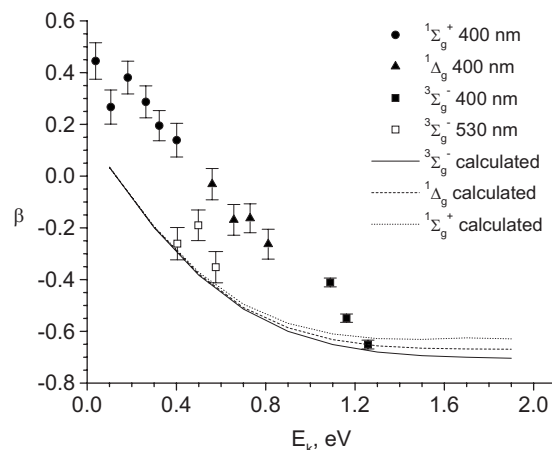


FIG. 16. Experimental (Ref. 96) and calculated (6-311G(2+)(3*df*)) anisotropy parameter for S_2^- .

puted anisotropies of all three states are very similar, as shown in Fig. 15. Calculations including FCF weighted contributions from all three states give rise to $\beta(E)$ dependence that resembles the behavior of the 396 nm data points; the three-state $\beta(E)$ is above the ground state O_2 curve. However, the changes in β with energy are much smaller. Thus, our calculations cannot explain the large difference between the $\beta(E)$ curves obtained at two different wavelengths. Interestingly, the calculations agree better with the 396 nm curve. A possible explanation is that the correlation and exchange interactions with the core are less important in the singlet states as compared to the triplets, and, consequently, the model employed here (which neglects the interactions between the detached electron and the core) works better for the cases when the photodetachment produces a neutral in a singlet state.

The experimental and calculated data for S_2^- are shown in Fig. 16. Experimental points were obtained in two experiments⁹⁶ using 400 and 530 nm wavelengths (3.10 and 2.34 eV, respectively) for photodetachment from the ground state of S_2^- . At 400 nm, three neutral states of S_2 are accessible: the ground state ($^3\Sigma_g^-$), and the first two excited states ($^1\Delta_g, ^3\Sigma_g^-$). At 530 nm only the ground state is observed. The photoelectron kinetic energy range available is different for each of the three states, such that the stars, solid triangles, and solid squares points in Fig. 16 should be part of three different $\beta(E)$ curves as they correspond to different ionization processes. However, the calculated $\beta(E)$ in Fig. 16 for the three ionization transitions (as well as the underlying Dyson orbitals) show even smaller differences (as compared to the isoelectronic O_2^- anion). This is consistent with the average sizes (X^2, Y^2, Z^2, R^2) of Dyson orbitals for different O_2 and S_2 states. For example, the ground state O_2 is 14.3% larger in X^2 than the second singlet state, while the corresponding S_2 states differ by 8.3%.

Overall, the computed anisotropy values are lower than the experimental values, even considering the relatively large experimental error bars. For the two excited states, the experimental $\beta(E)$ curves are parallel, while the ground state curve has a different slope. Note that in principle the open

and solid squares should be fitted to the same curve, as they both correspond to photodetachment producing S_2 in the ground state.

Another interesting feature is that β values at very low energies are around 0.4. The π^* -type Dyson orbital resembles a d orbital, for which the maximum β near threshold is 0.2. This is an analytical result for d -orbital and our calculated curves approach this value at low energies. Experimental values higher than 0.2 can be explained by deviations of the Dyson orbitals from an atomic d orbital, or the limitations of the model in which the interactions between the photoelectron and the core are neglected, as done in the present and the Cooper–Zare models. Our calculations, which use the actual Dyson orbital and numeric isotropic averaging, show that the deviations from an actual d orbital are negligible, i.e., the computed d and higher angular momentum contributions are indeed very small. It was suggested¹¹⁵ that S_2 is more polarizable, such that neutral core-photoelectron interactions determine changes in the symmetry of the core, while this effect is negligible in O_2 .

V. CONCLUSIONS

We presented calculations of the total and differential cross sections for photodetachment from negative ions using Dyson orbitals computed with EOM-CC wave functions and free wave description of the detached electron. The model does not use any empirical parameters. The energy dependence of the cross sections is reproduced well, however, the accuracy of absolute values varies. The maximum errors for F^- , C^- , NH_2^- , H^- , Li^- , and OH^- are 20%, although in many cases the computed cross sections are within experimental error bars. The largest errors are observed for O^- and O_2^- for which the calculated cross sections differ from the experimental ones by factor of 3 and 2, respectively.

For the atomic photodetachment, the assumptions of our model are the same as in the Cooper–Zare approach. Therefore, it is surprising that the calculated anisotropy parameters for atomic anions exhibit too slow decrease, which suggests that the diffuseness of the computed Dyson orbitals is underestimated. An incorrect asymptotic behavior is consistent with the artifactual oscillations of the Hartree–Fock and Dyson orbitals, and is probably due to the limitations of Gaussian basis sets.

The analysis of the Dyson orbitals in the case of O_2^- and S_2^- photodetachment shows very little differences between the orbitals corresponding to different states of the neutral. These small differences cannot explain the experimentally observed dependence of β on the energy of ionizing radiation. This suggests that the neglected interactions between the detached electron and the core may play an important role in shaping the angular distributions of photoelectrons. The experimental values of β at small energies in S_2^- , which exceed the asymptotic value of 0.2 allowed for this type of orbitals, also point out in this direction.

ACKNOWLEDGMENTS

We would like to thank Vadim A. Mozhayskiy for his help in developing the EZDYSON interface, to Evgeny

Epifanovsky for his help in parallelizing the code, and to Dr. Liang Tao for the helpful discussions. Support from the Department of Energy (Grant No. DE-FG02-05ER15685) is gratefully acknowledged. C.M.O. is a Wise postdoctoral fellow and acknowledges support from the Wise Research Fund (USC). This work is conducted under the auspices of the iOpenShell Center for Computational Studies of Electronic Structure and Spectroscopy of Open-Shell and Electronically Excited Species supported by the National Science Foundation through Grant No. CRIF:CRF CHE-0625419+0624602+0625237 grant. We are also grateful to the Institute of Mathematics and its Applications in Minnesota for its hospitality, computer resources, and productive environment during our stay at IMA as visiting scholars.

APPENDIX: ISOTROPIC AVERAGING PROCEDURE

Isotropic averaging is done by applying an inverse Euler rotation $\{\alpha\beta\gamma\}^{-1}$ transforming Dyson orbital from molecular to the lab frame, as described in Ref. 26. Here we give a few details about the choice of the angular grid used to generate an isotropic ensemble of molecular orientations in the lab frame.

Euler angles $\{\alpha\beta\gamma\}$ span the following ranges: $\alpha \in [0-2\pi[$, $\beta \in [0-\pi]$, and $\gamma \in [0-2\pi[$ and are uniquely defined, except for rotations by $\beta=0$ or π . In this case, the molecular and lab z -axis coincide, and α and γ rotations become equivalent. Thus, for $\beta=0$ or π , α spans the $[0-2\pi[$ range, while $\gamma=0$ only.

An isotropic grid is obtained by considering an equally spaced angular grid for the $\{\alpha\beta\gamma\}$ Euler angles. Alternatively, one can use equally spaced grids for α and γ rotations, while β rotations are chosen such that they are equally spaced in $\cos \beta$ (projection on the z -axis). We tested the averaging by using different initial orientations of the laser polarization with respect to the molecular frame and comparing the resulting total cross sections and anisotropy parameters. Our numeric integration tests show that an equally spaced angular grid for all three Euler angles gives better results when the same density angular grids are compared.

For any given $\{\alpha\beta\gamma\}$ orientation the weighting factor is given by the spherical surface area that it spans:

$$P(\alpha_i\beta_i\gamma_i) = \frac{\Delta\alpha\Delta\gamma}{2\pi} \frac{1}{2} (\cos \beta_{i+1} - \cos \beta_{i-1}). \quad (40)$$

¹M. Seel and W. Domcke, *J. Chem. Phys.* **95**, 7806 (1991).

²K. Wang and V. McKoy, *Annu. Rev. Phys. Chem.* **46**, 275 (1995).

³D. M. Neumark, *Annu. Rev. Phys. Chem.* **52**, 255 (2001).

⁴R. E. Continetti, *Annu. Rev. Phys. Chem.* **52**, 165 (2001).

⁵T. Seideman, *Annu. Rev. Phys. Chem.* **53**, 41 (2002).

⁶K. L. Reid, *Annu. Rev. Phys. Chem.* **54**, 397 (2003).

⁷A. Stolow, *Annu. Rev. Phys. Chem.* **54**, 89 (2003).

⁸A. Sanov and R. Mabbs, *Int. Rev. Phys. Chem.* **27**, 53 (2008).

⁹K. L. Reid, *Int. Rev. Phys. Chem.* **27**, 607 (2008).

¹⁰E. P. Wigner, *Phys. Rev.* **73**, 1002 (1948).

¹¹R. D. Mead, K. R. Lykke, and W. C. Lineberger, in *Electronic and Atomic Collisions*, edited by J. Eichler, I. V. Hertel, and N. Stolterfoht (Elsevier, New York, 1984), p. 721.

¹²T. A. Cool, J. Wang, K. Nakajima, C. A. Taatjes, and A. McIlroy, *Int. J. Mol. Sci.* **247**, 18 (2005).

- ¹³ C. A. Taatjes, S. J. Klippenstein, N. Hansen, J. A. Miller, T. A. Cool, J. Wang, M. E. Law, and P. R. Westmoreland, *Phys. Chem. Chem. Phys.* **7**, 806 (2005).
- ¹⁴ I. G. Kaplan, B. Barbiellini, and A. Bansil, *Phys. Rev. B* **68**, 235104 (2003).
- ¹⁵ E. Weigold and I. E. McCarthy, *Electron Momentum Spectroscopy* (Kluwer, Dordrecht, Plenum, New York, 1999).
- ¹⁶ M. S. Deleuze and S. Klippenberg, *J. Chem. Phys.* **125**, 104309 (2006).
- ¹⁷ S. Patchkovskii, Z. Zhao, T. Brabec, and D. M. Villeneuve, *Phys. Rev. Lett.* **97**, 123003 (2006).
- ¹⁸ J. Itatani, J. Levesque, D. Zeidler, H. Niikura, H. Pépin, J. C. Kieffer, P. B. Corkum, and D. M. Villeneuve, *Nature (London)* **432**, 867 (2004).
- ¹⁹ M. Yamazaki, T. Horio, N. Kishimoto, and K. Ohno, *Phys. Rev. A* **75**, 032721 (2007).
- ²⁰ A. A. Abrikosov, L. P. Gorkov, and J. E. Dzyaloshinski, *Methods of Quantum Field Theory in Statistical Physics* (Prentice-Hall, Englewood Cliffs, NJ, 1963).
- ²¹ A. L. Fetter and J. D. Walecka, *Quantum Theory of Many Particle Systems* (McGraw-Hill, New York, 1971).
- ²² J. V. Ortiz, *Adv. Quantum Chem.* **35**, 33 (1999).
- ²³ J. Linderberg and Y. Öhrn, *Propagators in Quantum Chemistry* (Academic, London, 1973).
- ²⁴ L. S. Cederbaum and W. Domcke, *Adv. Chem. Phys.* **36**, 205 (1977).
- ²⁵ L. S. Cederbaum, W. Domcke, J. Schrimmer, and W. von Niessen, *Adv. Chem. Phys.* **65**, 115 (1986).
- ²⁶ C. M. Oana and A. I. Krylov, *J. Chem. Phys.* **127**, 234106 (2007).
- ²⁷ D. J. Rowe, *Rev. Mod. Phys.* **40**, 153 (1968).
- ²⁸ T. H. Dunning and V. McKoy, *J. Chem. Phys.* **47**, 1735 (1967).
- ²⁹ T. H. Dunning and V. McKoy, *J. Chem. Phys.* **48**, 5263 (1968).
- ³⁰ T. I. Shibuya and V. McKoy, *J. Chem. Phys.* **53**, 3308 (1970).
- ³¹ C. W. McCurdy, T. N. Rescigno, D. L. Yeager, and V. McKoy, *Modern Theoretical Chemistry* (Plenum, New York, 1977), Vol. 3, pp. 339–386.
- ³² J. Simons and W. D. Smith, *J. Chem. Phys.* **58**, 4899 (1973).
- ³³ J. Simons, *Annu. Rev. Phys. Chem.* **28**, 15 (1977).
- ³⁴ T. T. Chen, J. Simons, and K. D. Jordan, *Chem. Phys.* **14**, 145 (1976).
- ³⁵ K. Emrich, *Nucl. Phys. A* **351**, 379 (1981).
- ³⁶ H. Sekino and R. J. Bartlett, *Int. J. Quantum Chem., Quantum Chem. Symp.* **26**, 255 (1984).
- ³⁷ J. Geertsen, M. Rittby, and R. J. Bartlett, *Chem. Phys. Lett.* **164**, 57 (1989).
- ³⁸ J. F. Stanton and R. J. Bartlett, *J. Chem. Phys.* **98**, 7029 (1993).
- ³⁹ S. V. Levchenko and A. I. Krylov, *J. Chem. Phys.* **120**, 175 (2004).
- ⁴⁰ D. Sinha, D. Mukhopadhyay, and D. Mukherjee, *Chem. Phys. Lett.* **129**, 369 (1986).
- ⁴¹ S. Pal, M. Rittby, R. J. Bartlett, D. Sinha, and D. Mukherjee, *Chem. Phys. Lett.* **137**, 273 (1987).
- ⁴² J. F. Stanton and J. Gauss, *J. Chem. Phys.* **101**, 8938 (1994).
- ⁴³ M. Nooijen and R. J. Bartlett, *J. Chem. Phys.* **102**, 3629 (1995).
- ⁴⁴ J. Simons, *Adv. Quantum Chem.* **50**, 213 (2005).
- ⁴⁵ D. Mukherjee and S. Pal, *Adv. Quantum Chem.* **20**, 291 (1989).
- ⁴⁶ R. J. Bartlett and J. F. Stanton, *Rev. Comput. Chem.* **5**, 65 (1994).
- ⁴⁷ R. J. Bartlett, *Int. J. Mol. Sci.* **3**, 579 (2002).
- ⁴⁸ J. F. Stanton and J. Gauss, *Adv. Chem. Phys.* **125**, 101 (2003).
- ⁴⁹ A. I. Krylov, *Acc. Chem. Res.* **39**, 83 (2006).
- ⁵⁰ O. Christiansen, *Theor. Chim. Acta* **116**, 106 (2006).
- ⁵¹ A. I. Krylov, *Annu. Rev. Phys. Chem.* **59**, 433 (2008).
- ⁵² H. J. Monkhorst, *Int. J. Quantum Chem., Quantum Chem. Symp.* **11**, 421 (1977).
- ⁵³ A. Landau and A. I. Krylov, “Frozen natural orbitals for ionized states within equation-of-motion coupled-cluster formalism,” *J. Chem. Phys.* (submitted).
- ⁵⁴ K. J. Reed, A. H. Zimmerman, H. C. Andersen, and J. I. Brauman, *J. Chem. Phys.* **64**, 1368 (1976).
- ⁵⁵ K. M. Ervin, I. Anusiewicz, P. Skurski, J. Simons, and W. C. Lineberger, *J. Phys. Chem. A* **107**, 8521 (2003).
- ⁵⁶ J. Simons, *J. Phys. Chem. A* **112**, 6401 (2008).
- ⁵⁷ A. Sanov and W. C. Lineberger, *Phys. Chem. Chem. Phys.* **6**, 2018 (2004).
- ⁵⁸ P. G. Wenthold and W. C. Lineberger, *Acc. Chem. Res.* **32**, 597 (1999).
- ⁵⁹ K. M. Ervin and W. C. Lineberger, in *Advances in Gas Phase Ion Chemistry*, edited by N. G. Adams and L. M. Babcock (JAP, Greenwich, CT, 1992), Vol. 1, pp. 121–166.
- ⁶⁰ J. V. Coe, S. M. Williams, and K. H. Bowen, *Int. Rev. Phys. Chem.* **27**, 27 (2008).
- ⁶¹ W. J. Zheng, J. M. Nilles, D. Radisic, S. T. Stokes, B. A. Trotter, S. Eustis, A. Grubisic, X. Li, and K. H. Bowen, in *Proceedings of the INDO-US Conference on Materials and Biological Applications*, edited by S. N. Saku, R. K. Choudhury, and P. Jena (Nova, New York, 2006), p. 135.
- ⁶² O. T. Ehrler and D. M. Neumark, *Acc. Chem. Res.* **42**, 769 (2009).
- ⁶³ D. M. Neumark, *J. Phys. Chem. A* **112**, 13287 (2008).
- ⁶⁴ A. N. Alexandrova, J. C. Bopp, B. M. Elliott, T. Herden, and M. A. Johnson, *Int. J. Mol. Sci.* **283**, 94 (2009).
- ⁶⁵ S. Horvath, A. McCoy, J. R. Roscioli, and M. A. Johnson, *J. Phys. Chem. A* **112**, 12337 (2008).
- ⁶⁶ R. A. Relph, J. C. Bopp, and M. A. Johnson, *J. Chem. Phys.* **129**, 064305 (2008).
- ⁶⁷ H. Schneider, J. M. Weber, E. M. Myshakin, K. D. Jordan, J. Bopp, T. Herden, and M. A. Johnson, *J. Chem. Phys.* **127**, 084319 (2007).
- ⁶⁸ J. C. Bopp, J. R. Roscioli, M. A. Johnson, T. M. Miller, A. A. Viggiano, S. M. Villano, S. W. Wren, and W. C. Lineberger, *J. Phys. Chem. A* **111**, 1214 (2007).
- ⁶⁹ W. H. Robertson and M. A. Johnson, *Annu. Rev. Phys. Chem.* **54**, 173 (2003).
- ⁷⁰ K. H. Bowen and E. W. Schlag, in *The Encyclopedia of Mass Spectrometry*, edited by P. Armentrout (Elsevier, Amsterdam, 2003), Vol. 1, p. 736.
- ⁷¹ D. M. Neumark, *J. Chem. Phys.* **125**, 132303 (2006).
- ⁷² D. M. Neumark, *Phys. Chem. Chem. Phys.* **7**, 433 (2005).
- ⁷³ A. Stolow, A. E. Bragg, and D. M. Neumark, *Chem. Rev. (Washington, D.C.)* **104**, 1719 (2004).
- ⁷⁴ J. Simons, in *Photoionization and Photodetachment*, Advanced Series in Physical Chemistry Vol. 10, edited by C. Y. Ng (World Scientific, Singapore, 2000).
- ⁷⁵ J. Cooper and R. N. Zare, *J. Chem. Phys.* **48**, 942 (1968).
- ⁷⁶ S. T. Manson and A. F. Starace, *Rev. Mod. Phys.* **54**, 389 (1982).
- ⁷⁷ D. Dill, S. T. Manson, and A. F. Starace, *Phys. Rev. Lett.* **32**, 971 (1974).
- ⁷⁸ J. Cooper and R. N. Zare, *J. Chem. Phys.* **49**, 4252 (1968).
- ⁷⁹ A. F. Starace, R. H. Rast, and S. T. Manson, *Phys. Rev. Lett.* **38**, 1522 (1977).
- ⁸⁰ S. N. Dixit and V. McKoy, *J. Chem. Phys.* **82**, 3546 (1985).
- ⁸¹ K. L. Reid, D. J. Leahy, and R. N. Zare, *J. Chem. Phys.* **95**, 1746 (1991).
- ⁸² D. J. Leahy, K. L. Reid, and R. N. Zare, *J. Chem. Phys.* **95**, 1757 (1991).
- ⁸³ H. Park and R. N. Zare, *J. Chem. Phys.* **104**, 4554 (1996).
- ⁸⁴ P. Hockett and K. L. Reid, *J. Chem. Phys.* **127**, 154308 (2007).
- ⁸⁵ R. M. Stehman and S. B. Woo, *Phys. Rev. A* **20**, 281 (1979).
- ⁸⁶ R. R. Lucchese, G. Raseev, and V. McKoy, *Phys. Rev. A* **25**, 2572 (1982).
- ⁸⁷ I. Powis, *Chem. Phys.* **201**, 189 (1995).
- ⁸⁸ N. A. Cherepkov, S. K. Semenov, Y. Hikosaka, K. Ito, and A. Yaghisita, *Phys. Rev. Lett.* **84**, 250 (2000).
- ⁸⁹ I. Cacelli, R. Moccia, and A. Rizzo, *Phys. Rev. A* **57**, 1895 (1998).
- ⁹⁰ H. A. Bethe and E. E. Salpeter, *Quantum Mechanics of One and Two Electron Atoms* (Plenum, New York, 1977).
- ⁹¹ B. T. Pickup and O. Goscinsky, *Mol. Phys.* **26**, 1013 (1973).
- ⁹² B. T. Pickup, *Chem. Phys.* **19**, 193 (1977).
- ⁹³ J. J. Sakurai, *Modern Quantum Mechanics* (Addison-Wesley, Reading, MA, 1995).
- ⁹⁴ H. A. Bethe, *Phys. Rev.* **93**, 888 (1954).
- ⁹⁵ J. Cooper and R. N. Zare, in *Atomic Collision Processes*, edited by S. Geltman, K. T. Mahanthappa, and W. E. Brittin (Gordon and Breach, New York, 1968), Vol. 11C, p. 317.
- ⁹⁶ E. Surber, R. Mabbs, and A. Sanov, *J. Phys. Chem. A* **107**, 8215 (2003).
- ⁹⁷ F. A. Akin, L. K. Schirra, and A. Sanov, *J. Phys. Chem. A* **110**, 8031 (2006).
- ⁹⁸ Y. Shao, L. F. Molnar, Y. Jung, J. Kussmann, C. Ochsenfeld, S. Brown, A. T. B. Gilbert, L. V. Slipchenko, S. V. Levchenko, D. P. O’Neil, R. A. Distasio, Jr., R. C. Lochan, T. Wang, G. J. O. Beran, N. A. Besley, J. M. Herbert, C. Y. Lin, T. Van Voorhis, S. H. Chien, A. Sodt, R. P. Steele, V. A. Rassolov, P. Maslen, P. P. Korambath, R. D. Adamson, B. Austin, J. Baker, E. F. C. Bird, H. Daschel, R. J. Doerksen, A. Drew, B. D. Dunietz, A. D. Dutoi, T. R. Furlani, S. R. Gwaltney, A. Heyden, S. Hirata, C.-P. Hsu, G. S. Kedziora, R. Z. Khallilulin, P. Klunzinger, A. M. Lee, W. Z. Liang, I. Lotan, N. Nair, B. Peters, E. I. Proynov, P. A. Pieniazek, Y. M. Rhee, J. Ritchie, E. Rosta, C. D. Sherrill, A. C. Simmonett, J. E. Subotnik, H. L. Woodcock III, W. Zhang, A. T. Bell, A. K. Chakraborty, D. M. Chipman, F. J. Keil, A. Warshel, W. J. Herhe, H. F. Schaefer III, J. Kong, A. I. Krylov, P. M. W. Gill, and M. Head-Gordon, *Phys. Chem. Chem. Phys.* **8**, 3172 (2006).

- ⁹⁹ MOLPRO, a package of *ab initio* programs designed by H.-J. Werner and P. J. Knowles, version 2002.6.
- ¹⁰⁰ W. J. Hehre, R. Ditchfield, and J. A. Pople, *J. Chem. Phys.* **56**, 2257 (1972).
- ¹⁰¹ R. Krishnan, J. S. Binkley, R. Seeger, and J. A. Pople, *J. Chem. Phys.* **72**, 650 (1980).
- ¹⁰² T. H. Dunning, *J. Chem. Phys.* **90**, 1007 (1989).
- ¹⁰³ M. Gutowski, K. D. Jordan, and P. Skurski, *J. Phys. Chem. A* **102**, 2624 (1998).
- ¹⁰⁴ C. M. Oana, V. A. Mozhayskiy, and A. I. Krylov, EZDYSON, <http://iopenshell.usc.edu/downloads/>.
- ¹⁰⁵ See EPAPS supplementary material <http://dx.doi.org/10.1063/1.3231143> for cross-section and anisotropy outputs from the EZDYSON program.
- ¹⁰⁶ V. A. Mozhayskiy and A. I. Krylov, EZSPECTRUM, <http://iopenshell.usc.edu/downloads/>.
- ¹⁰⁷ J. Hachmann, P. T. A. Galek, T. Yanai, G. K. L. Chan, and N. C. Handy, *Chem. Phys. Lett.* **392**, 55 (2004).
- ¹⁰⁸ C. D. Sherrill, A. I. Krylov, E. F. C. Byrd, and M. Head-Gordon, *J. Chem. Phys.* **109**, 4171 (1998).
- ¹⁰⁹ L. M. Branscomb, D. S. Burch, S. J. Smith, and S. Geltman, *Phys. Rev.* **111**, 504 (1958).
- ¹¹⁰ L. M. Branscomb, S. J. Smith, and G. Tisone, *J. Chem. Phys.* **43**, 2906 (1965).
- ¹¹¹ J. Dellwo, Y. Liu, and D. J. Pegg, *Phys. Rev. A* **45**, 1544 (1992).
- ¹¹² G. Haefliger, D. Hanstorp, I. Kiyani, A. E. Klinkmuller, U. Ljungblad, and D. J. Pegg, *Phys. Rev. A* **53**, 4127 (1996).
- ¹¹³ H. J. Kaiser, E. Heinicke, R. Rackwitz, and D. Feldmann, *Z. Phys.* **270**, 259 (1974).
- ¹¹⁴ D. S. Burch, S. J. Smith, and L. M. Branscomb, *Phys. Rev.* **112**, 171 (1958).
- ¹¹⁵ A. Sanov, private communication.
- ¹¹⁶ C. Blondel, P. Cacciani, C. Delsart, and R. Trainham, *Phys. Rev. A* **40**, 3698 (1989).
- ¹¹⁷ C. Blondel, C. Delsart, and F. Goldfarb, *J. Phys. B* **34**, L281 (2001).
- ¹¹⁸ M. Scheer, R. C. Bilodeau, C. A. Brodie, and H. K. Haugen, *Phys. Rev. A* **58**, 2844 (1998).
- ¹¹⁹ C. Valli, C. Blondel, and C. Delsart, *Phys. Rev. A* **59**, 3809 (1999).
- ¹²⁰ C. L. Pekeris, *Phys. Rev.* **126**, 1470 (1962).
- ¹²¹ K. R. Lykke, K. K. Murray, and W. C. Lineberger, *Phys. Rev. A* **43**, 6104 (1991).
- ¹²² L. M. Branscomb, *Phys. Rev.* **148**, 11 (1966).
- ¹²³ *CRC Handbook of Chemistry and Physics*, 62th ed., edited by R. C. Weast (CRC Press, Boca Raton, FL, 1981).
- ¹²⁴ K. C. Smyth and J. I. Brauman, *J. Chem. Phys.* **56**, 4620 (1972).
- ¹²⁵ A. Mandl, *Phys. Rev. A* **3**, 251 (1971).
- ¹²⁶ M. L. Sernan and L. M. Branscomb, *Phys. Rev.* **125**, 1602 (1962).
- ¹²⁷ S. J. Smith and D. S. Burch, *Phys. Rev.* **116**, 1125 (1959).
- ¹²⁸ D. Hanstorp, C. Bengtsson, and D. J. Larson, *Phys. Rev. A* **40**, 670 (1989).
- ¹²⁹ A. M. Covington, D. Calabrese, W. W. Williams, J. S. Thompson, and T. J. Kvale, *Phys. Rev. A* **56**, 4746 (1997).